## MATERIALS SCIENCE

# Tailor-made temperature-dependent thermal conductivity via interparticle constriction

Fabian A. Nutz and Markus Retsch*

Managing heat is a major challenge to meet future demands for a sustainable use of our energy resources. This requires materials, which can be custom-designed to exhibit specific temperature-dependent thermal transport properties to become integrated into thermal switches, transistors, or diodes. Common crystalline and amorphous materials are not suitable, owing to their gradual changes of the temperature-dependent thermal conductivity. We show how a second-order phase transition fully controls the temperature-dependent thermal transport properties of polymer materials. We demonstrate four major concepts based on a colloidal superstructure: (i) control of transition temperature, (ii) width of phase transition regime, (iii) multistep transitions, and (iv) step height of the transition. Most importantly, this unique control over thermal conductivity is only governed by the interparticle constriction, the particle composition, and its mesostructure. Our concept is therefore also applicable to a wide variety of other particulate materials.

## INTRODUCTION

With increasing energy consumption and further miniaturization of electronic devices, a need for new, space-saving, and functional materials to manage heat arises. Recent examples report on the theory and realization of thermal memory (1–3), thermal rectification (4–6), dynamic insulation (7, 8), phase change materials (9), thermal cloaking (10), and thermal switching materials (11). The experimental realization of many of these emerging applications is still a great challenge. One major limiting factor is given by the typical power-law temperature dependence of the thermal conductivity of most materials. For crystalline materials, one usually finds a power-law exponent of +3 up to the point where phonon-phonon scattering dominates (~10% of the Debye temperature). Beyond that point, a −1 to −3 exponent is found for increasing temperatures (12). Amorphous materials merely exhibit a monotonic increase across the entire temperature range, combined with commonly one or two plateau regimes (13). To pave the way toward advanced heat management devices and thermal logic circuits, tailor-made materials with non–power-law but well-controlled temperature-dependent properties are needed. For example for thermal diodes, nonlinearity is required (12), whereas abrupt changes with a small input of excess heat are necessary for the gate material of thermal transistors (14). State-of-the-art materials use a first-order phase transition either in their homogeneous bulk form (9, 14–17) or in a heterogeneous blend (18–21) to manipulate the temperature-dependent thermal transport. In homogeneous bulk materials, the thermal properties are governed by the material composition, rendering it difficult to target a specific application. Composite materials provide a higher degree of flexibility, owing to the selection of certain material combinations.

Quite importantly, the temperature-dependent properties of a material can additionally be strongly influenced by the underlying micro- and nanostructure (22, 23). Prime examples are colloidal crystals, which have received much attention, predominantly within the field of photonics (24–27), phononics (25, 28, 29), or as template structures (30–32). Highly defined colloidal superstructures are accessible in a simple and scalable way by established fabrication methods (30–32). Colloidal crystals represent a significantly underexplored field with re-spect to their thermal transport properties. When going through the second-order phase transition, namely, the glass transition temperature of the constituting polymer, the increase in polymer mobility leads to a loss of the particulate nanostructure. Consequently, the thermal conductivity increases sharply (33). The versatile structural fabrication can be complemented by specific particle design to add further functionality to the colloidal ensemble. This allows to widely program the thermal transport properties to a specific need.

Here, we demonstrate the vast potential of constriction-controlled thermal transport through particulate ensembles. We choose polymer colloidal crystals as a case study to specifically tune temperature-dependent thermal conductivity. We emphasize that this tuning is solely based on geometric constriction. Precisely, thermal conductivity is governed by the thermally induced changes of the nanosized interparticle contact area between adjacent particles in a close-packed colloidal superstructure. Figure 1 outlines the unique possibilities provided by constriction-controlled thermal transport. We demonstrate four key aspects, which are of paramount importance for future heat management devices and become accessible for the first time via our concept: (i) adjustment of the (second-order) phase transition to a desired temperature (Fig. 1B); (ii) tuning of the phase transition range (Fig. 1C); (iii) introduction of multiple discrete transition steps (Fig. 1D); and (iv) controlling of the degree of transition change (Fig. 1E).

We show how to program the described transition behavior of these assemblies by adjusting the thermal properties of the polymer particles and by selecting a suitable mesoscopic colloidal crystal architecture. Our system is based on copolymer particles consisting of $n$-butyl methacrylate ($n$-BA) and methyl methacrylate (MMA). By adjusting the $n$-BA content of the particles, it is possible to control the glass transition temperature of the copolymer (26).

## RESULTS

### Adjustment of the phase transition to the desired temperature

We start by tailoring the onset transition temperature of the thermally inducible increase of the thermal conductivity. Therefore, highly monodisperse $n$-BA-co-MMA particles having different glass transition temperatures and a nearly equal diameter (182 to 223 nm; table S1, set-1) were synthesized. The particle self-assembly typically yields

Department of Chemistry, University of Bayreuth, Universitaetsstraße 30, 95447 Bayreuth, Germany.
*Corresponding author. Email: markus.retsch@uni-bayreuth.de
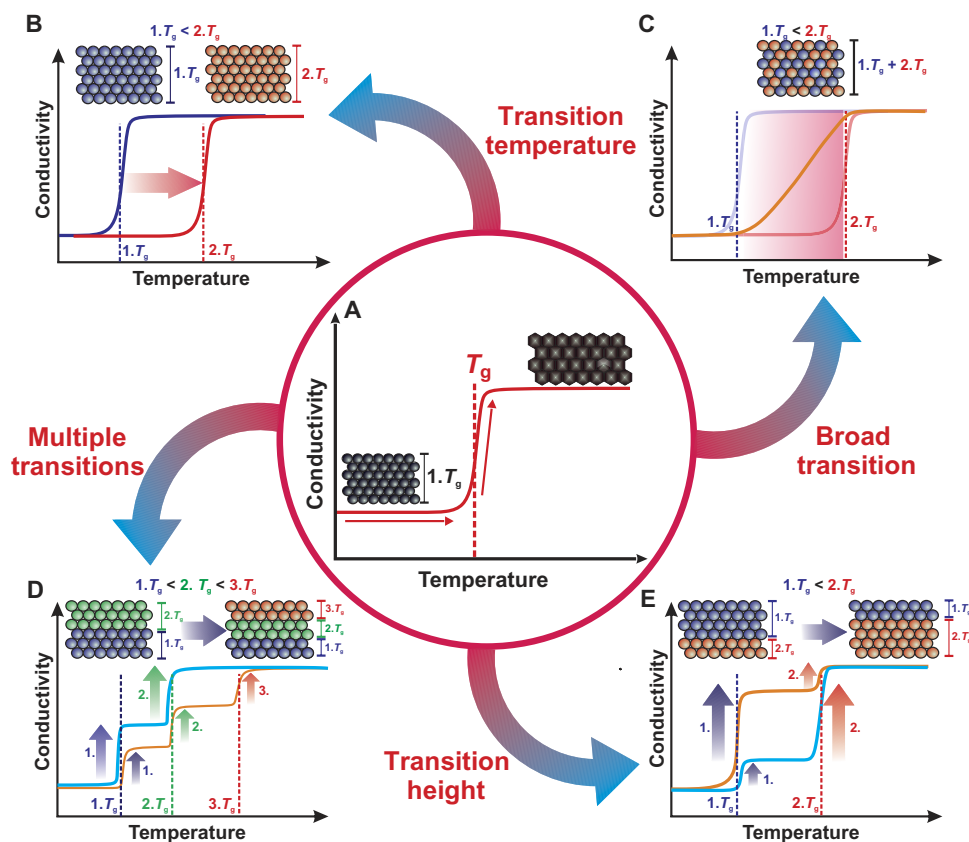
**Fig. 1. Key aspects for heat management devices and their realization based on constriction-controlled thermal transport in colloidal assembly structures.** (**A**) By exceeding $T_g$, the thermal conductivity irreversibly increases based on the enlargements of contact points during particle sintering. (**B**) The transition temperature can be tailored by assembling the crystal from particles having different $T_g$. (**C**) The random coassembly of equal-sized particles but different $T_g$ results in a broad transition. (**D**) Multiple transition steps can be introduced by a discrete layer-by-layer assembly. (**E**) The height of the transition steps is controllable by the thickness of the respective layer.

freestanding disk-shaped monoliths with a diameter of ~20 mm and a thickness of several hundred micrometers. Optical and scanning electron microscopy (SEM) images of the split edges of these monoliths are shown in Fig. 2A.

A strong opalescence is visible throughout the entire monoliths based on Bragg reflection (*34, 35*). This indicates a high-crystalline order of the particles within the specimen. Different reflectivity colors within a monolith arise from various crystal planes exposed to the surface. The slightly varying colors between the different monoliths are based on the size dependency of the Bragg reflection. SEM images confirm the optical microscopy impression. The polymer particles arrange into a well-defined, close-packed face-centered cubic symmetry. Overall, the samples can be regarded as fully crystalline.

Figure 2B shows the temperature-dependent heat capacity of the synthesized copolymers with a varying MMA content of 70, 80, 90, and 100%. The absolute heat capacity increases with increasing *n*-BA content. The systematic shift of the glass transition from 54°C (70 volume % MMA) to 127°C (100% MMA) further proves the successful random copolymerization. In general, copolymers having a glass transition temperature between the $T_g$ of pure poly(*n*-BA) (−49°C) and pure poly(MMA) (125°C) are accessible via the random copolymerization of these two monomers. This leaves ample degrees of freedom to tailor the temperature response toward specific needs in a broad ambient temperature range.

The thermal conductivity data are summarized in Fig. 2C. All samples show a sharp, step-like increase of the thermal conductivity near the glass transition temperature of the corresponding polymer. At this point, the interparticle contact points enlarge and the porosity within the sample vanishes, resulting in a strongly increased thermal conductivity. The kinetics of this transition have been examined elsewhere (*36*). In all cases, a sharp increase in thermal conductivity by at least 200% could be programmed to a specific temperature, simply by controlling the second-order phase transition of the constituting polymer. The effective thermal conductivity through a colloidal crystal depends on the size of the constituting latex particles. This will be investigated and discussed in another contribution. However, the width of the step-like transition is hardly affected by the particle size, which can also be inferred from a previous publication (*33*). To rule out size effects as much as possible, we only worked with two sets of particles with sizes around 200 and 420 nm.

## Tuning of the phase transition range
For a seamless adjustment of the thermal conductivity between the pristine (<100 mW m$^{-1}$ K$^{-1}$) and the sintered state (>200 mW m$^{-1}$ K$^{-1}$), a random coassembly of two particle types with comparable size can be used (Fig. 3A).

We demonstrate this capability with a $T_{g,2}$ = 103°C and $T_{g,1}$ = 61°C particle with 403- and 434-nm diameters, respectively. The indicated
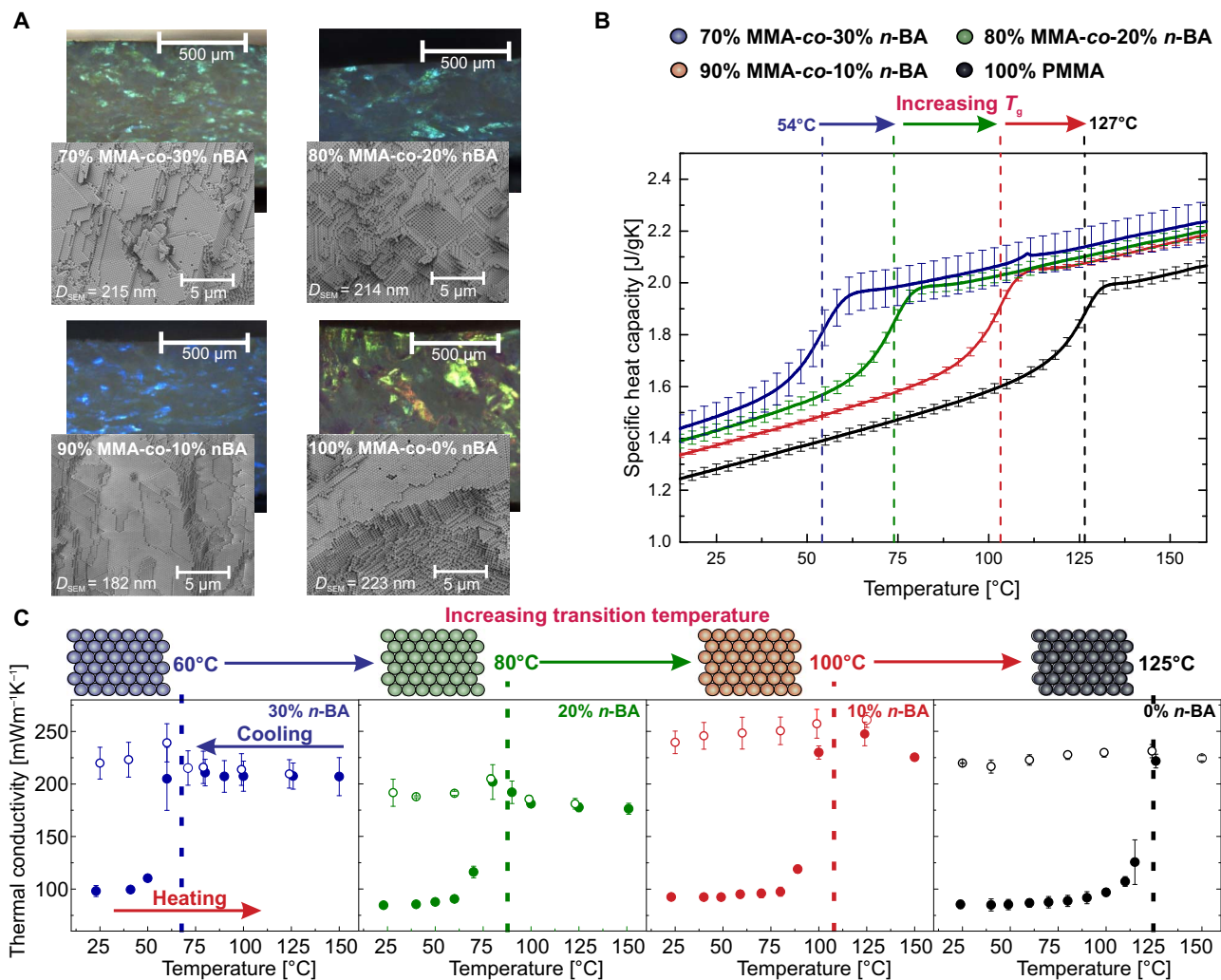
**Fig. 2. Thermal conductivity of polymer colloidal crystals having different $T_g$.** (**A**) Optical and SEM images of the split edges of the assembled crystals. The strong opalescence indicates a long-range crystalline order within the freestanding monoliths. The high crystallinity is confirmed by the corresponding SEM images. (**B**) Specific heat capacity of the synthesized copolymer particles. With increasing MMA content, the $T_g$ of the polymer is shifted to higher temperatures. (**C**) Temperature-dependent thermal conductivity of polymer colloidal crystals from particles having different $T_g$ (heating and cooling cycle). By adjusting the copolymer composition, it is possible to tailor the transition temperature systematically. Error bars represent the SD derived from three individual measurements. Closed symbols represent the heating cycle; open symbols represent the cooling cycle.

particle ratios represent number mixing ratios of the binary particle dispersions. Number and volume ratios can be treated equivalently here due to the comparable particle size and density. Because of the almost equal size of the particles, the overall crystallinity of the colloidal ensemble is preserved. This can be inferred from the bright opalescent colors in the side-view optical micrographs (Fig. 3B). The initial and final temperature of the transition can be freely chosen on the basis of the $T_g$ of the constituting particles. Whereas the crystals made from only one particle type (Fig. 3C, blue/red) show the familiar sharp increase in thermal conductivity, the coassembled colloidal crystal shows a broad, linear increase from the lower to the higher $T_g$ (Fig. 3C, orange circles). This trend is also readily confirmed in the thermal diffusivity data (fig. S3). It is therefore inherent to thermal transport changes within the colloidal crystal and does not originate from variations in the density or specific heat capacity used to calculate thermal conductivity [differential scanning calorimetry (DSC) data are given in fig. S1]. We ascribe this broad transition to the following reason. By exceeding the first $T_g$, the

lower $T_g$ particles deform and thereby increase the contact area to the surrounding higher $T_g$ particles. In addition, clusters and probably percolating trusses of the already softened component may form at this stage. Still, a skeleton of the higher $T_g$ particles partially retain the structure and prevents a sharp increase of the thermal conductivity. By further increasing the temperature, the lower $T_g$ particles become softer, and the polymer chains become more mobile. This can lead to a further increase of the interparticle contact area and progressively results in a dense film formation. In addition, the softening of the higher $T_g$ particles starts to set in. Ultimately, by exceeding the glass transition temperature of the higher $T_g$ particle, the remaining structure vanishes completely, and the bulk thermal conductivity of the polymer film (~200 mW m$^{-1}$ K$^{-1}$) is obtained. The gradual film formation process can be inferred from SEM cross section images recorded after annealing at 60°, 80°, and 100°C (fig. S6). Thus, a continuous adjustment of the thermal conductivity is possible via a simple binary colloidal crystal and the gradual loss of the constricting interparticle contact points. Note
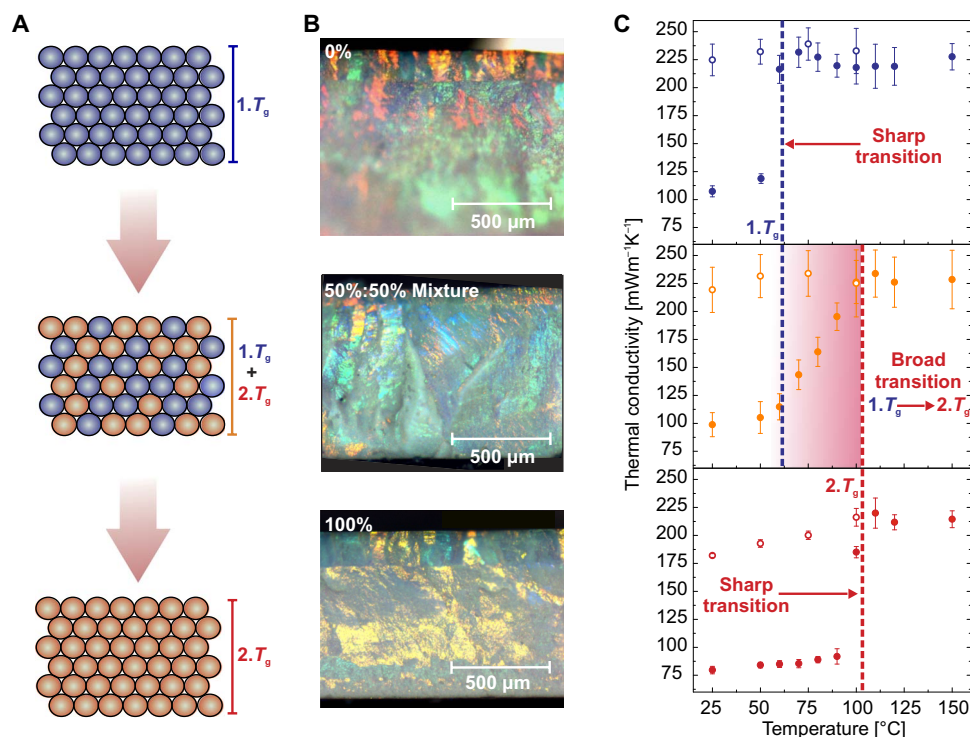
**Fig. 3. Temperature-dependent thermal conductivity of coassembled polymer colloidal assemblies.** (**A**) Schematic illustration of the composition of a coassembled colloidal crystal. The coassembly leads to structurally homogeneous colloidal crystals due to the comparable particle size. (**B**) Optical micrographs of the split edges of pure colloidal crystals (mixing ratios, 0 and 100% of $T_g = 103°C$ particles) in comparison to a coassembled binary crystal (mixing ratio, 50%:50%). (**C**) Temperature-dependent thermal conductivity of the 50%:50% colloidal crystal compared to its pure counterparts. The binary colloidal crystal shows a broad transition, ranging between the glass transition temperatures (dashed lines) of the pure copolymer particles. Error bars represent the SD derived from three individual measurements. Thermal diffusivity data can be found in fig. S3A. Closed symbols represent the heating cycle; open symbols represent the cooling cycle.

that we also prepared binary colloidal crystals with various mixing ratios (fig. S4). However, these retain a sharp transition feature at the $T_g$ of the majority component. This hints toward the importance of cluster and percolation formation, which we observed for the 50%:50% mixture.

## Introduction of multiple discrete transition steps

To program distinct steps into the temperature-dependent thermal conductivity, we fabricated more intricate colloidal superstructures. Therefore, we used filtration, which easily allows fabricating layered colloidal ensembles. Filtration represents a much faster self-assembly method compared to the evaporation-induced self-assembly. However, this comes at the expense of the long-range crystalline order (fig. S5A). Nevertheless, filtration provides direct access to tailor-made colloidal superstructures in a layer-by-layer fashion. Thus, we fabricated multi-layered, freestanding colloidal monoliths in which every layer consisted of particles with a predefined $T_g$. We demonstrate the thermal transport properties of three particles of ~420-nm diameter with $T_{g,1} = 61°C$, $T_{g,2} = 103°C$, and $T_{g,3} = 124°C$. This introduces multiple transition steps of the thermal conductivity by a discrete sintering of the individual layers at the respective $T_g$. The schematic structure for these monoliths is illustrated in Fig. 4A.

The temperature-dependent thermal conductivity of colloidal assemblies consisting of one, two, and three particle layers is illustrated in Fig. 4B. In contrast to the randomly mixed binary colloidal crystal discussed above (Fig. 3), the discrete layer assembly evokes distinct steps in the thermal conductivity profile. This is based on the sintering of the homogenous, individual layer at its corresponding $T_g$. The unmolten

layers remain in their pristine state. Exceeding the $T_g$ of the remaining layers results in a further, multistep increase of the effective thermal conductivity of the entire ensemble. Conceptually, an arbitrary number of distinct steps could be introduced in this fashion to a particulate material. We demonstrate a three-step material by layering three particle types. The respective transition temperatures coincide with the predetermined $T_g$ (Fig. 4B, orange).

## Controlling the degree of transition change

Finally, it is also important to control how much thermal conductivity will change upon crossing a specific temperature. Building upon our experience of the multilayered structure introduced above, we conceived a suitable colloidal architecture. This is achieved by adjusting the layer thicknesses within a two-layer assembly. The structure of these assemblies is schematically sketched in Fig. 5A. Our sample consists of two particles ($T_{g,1} = 61°C$ and $T_{g,2} = 124°C$).

On the basis of the amount of particle dispersion used in the filtration process, it is readily possible to adjust the thicknesses of the different layers within the final assembly. Figure 5B shows the temperature-dependent thermal conductivity of three different colloidal assemblies with varying thickness ratios between both particle layers. The layer thickness of the higher $T_g$ particle layer increases from left to right.

Although a strong increase of the thermal conductivity at the lower glass transition temperature (Fig. 5B, left, blue arrow) is visible for monoliths containing only a thin layer of high $T_g$ particles, this behavior reverses for assemblies containing a thick layer of high $T_g$ particles (Fig. 5B, right, red arrow). Consequently, this concept allows for a
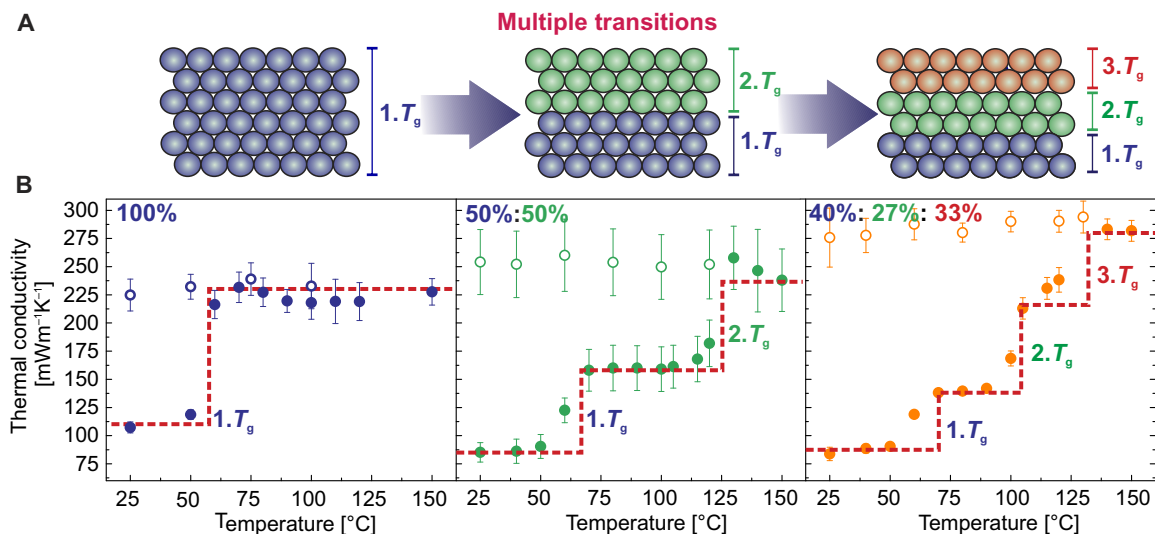
**Fig. 4. Introduction of multiple-step transitions.** (**A**) Schematic illustration of the structure of a colloidal monolith consisting of one, two, and three particle layers where each layer has a different $T_g$ (blue, green, and red). (**B**) Temperature-dependent thermal conductivity of colloidal monoliths consisting of one, two, and three particle layers. On the basis of the discrete layer assembly, multiple step-like increases (dashed red lines) at the specific $T_g$ of the copolymer particle are observed. Error bars represent the SD derived from three individual measurements. Thermal diffusivity data can be found in fig. S3 (A and B). Closed symbols represent the heating cycle; open symbols represent the cooling cycle.
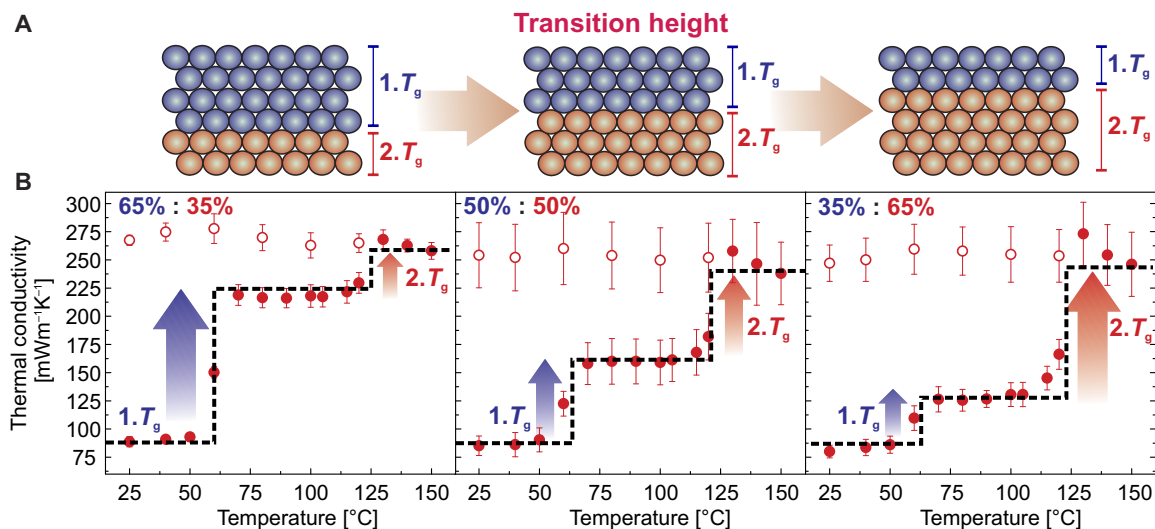


**Fig. 5. Tuning the transition height.** (**A**) Schematic illustration of the structure of a colloidal monolith with varying layer thickness. The thickness of the red particle layer increases from left to right. (**B**) Temperature-dependent thermal conductivity of different colloidal assemblies with varying particle layer thickness. The thickness of the higher $T_g$ layer is increased from left to right, leading to an increasing transition height at the second $T_g$ (red arrow). Error bars represent the SD derived from three individual measurements. Thermal diffusivity data can be found in fig. S3 (D and E). Closed symbols represent the heating cycle; open symbols represent the cooling cycle.

precise adjustment of the target thermal conductivity after exceeding a specific temperature—simply by controlling the relative amount of material changing from insulating to a more conducting state. Furthermore, this could also be extended to three or more layers.

Finally, we want to demonstrate that the four fundamental concepts outlined so far can be combined with each other. This gives even more degrees of freedom to design any specific temperature-dependent thermal conductivity profile. We therefore chose a two-layer assembly, combining the evaporation-induced self-assembly of a random mixture with the filtration-aided buildup of a layered structure. A schematic

sketch of the intended colloidal architecture is shown in Fig. 6, as well as the temperature-dependent thermal conductivity of such an assembly. Optical microscopy images of this structure are shown in fig. S5B.

The bottom layer consists of a crystalline coassembly of two equally sized particles with $T_{g,1} = 103°C$ and $T_{g,2} = 61°C$ (equal to the assembly shown in Fig. 3C). The top layer comprises only one particle type $T_{g,3} = 127°C$ and is not crystalline due to the faster filtration self-assembly process. With this architecture, it is possible to tailor the thermal conductivity to show a broad transition between 60° and 100°C, analogous
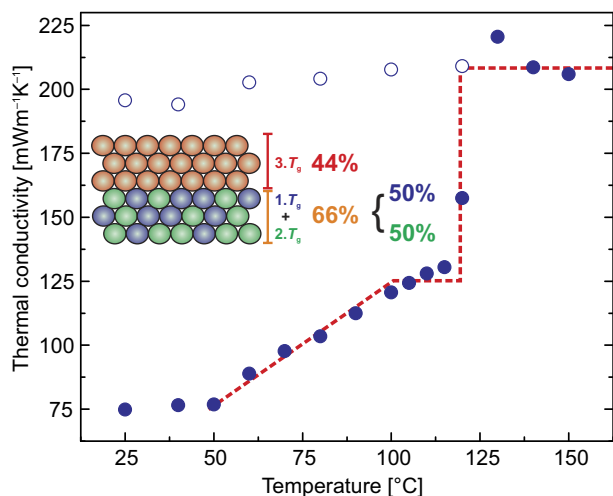
**Fig. 6. Combining a broad and a step-like transition.** Temperature-dependent thermal conductivity of a two-layer colloidal assembly. Whereas the bottom layer is fabricated by evaporation-induced self-assembly of two particles having different $T_g$ (90 volume % MMA-2, $T_g$ = 103°C; 70 volume % MMA-2, $T_g$ = 61°C), the upper layer consists of only one particle type (100 volume % MMA-1, $T_g$ = 127°C). Thermal diffusivity data can be found in fig. S3F. Closed symbols represent the heating cycle; open symbols represent the cooling cycle.

to Fig. 3, and a sharp, step-like increase of the thermal conductivity at ~125°C, similar to Fig. 2. The respective step heights are governed by the relative layer thicknesses of the two components.

## DISCUSSION

These four concepts show that colloidal assembly structures can control the temperature-dependent thermal transport properties with an unprecedented degree of flexibility. This capability becomes even more relevant because the fabrication method is scalable and can be flexibly adapted to other materials too. This allows introduction of further functional properties. Furthermore, the constriction-controlled thermal transition represents a purely solid-state transition, with no liquids involved. Although the polymer platform presented here does not allow a reversible adjustment of the thermal properties, we are convinced that this concept can be expanded to other material systems too. These may then provide the required reversibility for future applications. Our findings outline a general approach to specifically tailor the temperature-dependent thermal conductivity of a nanostructured material. We want to stress the high relevance of the interparticle contact points, which is the first ingredient to allow this impressive degree of flexibility. The ability to adjust the onset of the glass transition temperature of the polymer particles by simple chemical synthesis is the second key ingredient. Combining these two parameters in a tailor-made colloidal superstructure allowed us to show four key properties, which will be of relevance for future heat management devices: (i) adjustable onset temperature, (ii) width of transition, (iii) multistep transitions, and (iv) height of transition steps. However, one also has to consider the current shortcoming of this simple material composition, namely, the irreversibility of changes to the interparticle contact area. Nevertheless, we are convinced that this contribution will motivate more research on thermal transport through particulate structures. This may very likely lead to the availability of more functional particle compositions, which may circumvent the irreversibility of the polymer particle

sintering. Furthermore, these may allow for the introduction of other external stimuli, such as pH, solvents, light, electric currents, or electric fields to trigger the necessary transition. Considering the inherent and well-known photonic and phononic properties of colloidal crystals and glasses adds even another dimension of functionality, which we did not elaborate on in this contribution. Thus, this concept paves the way toward a genuinely multiphysical and multifunctional heat management material.

## MATERIALS AND METHODS

MMA (99%; Sigma-Aldrich) and $n$-BA (≥99%; Sigma-Aldrich) were purified by filtration over an alumina column (activated, basic, Brockmann I, Sigma-Aldrich). Potassium peroxodisulfate (KPS; ≤99%; Sigma-Aldrich), 4-styrenesulfonic acid sodium salt hydrate (99%; Sigma-Aldrich), and acrylic acid (AA; 99%; Sigma-Aldrich) were used as received. Ultrapure water was taken from a Millipore Direct-Q 3 UV unit and was used throughout the entire synthesis.

### Particle synthesis
Polymer particles were synthesized by emulsifier-free emulsion polymerization ($37, 38$). In a typical synthesis, 50 ml of the monomer mixture (for example, 40-ml MMA/10-ml $n$-BA for 20 volume % $n$-BA particles) and 450 ml of ultrapure water were charged in a three-necked flask, heated to 75°C, and equilibrated for 15 min under a slight argon flow. Subsequently, 2 ml of AA was added to the mixture followed by a further equilibration step of 5 min. The polymerization was initiated by adding 150 mg of KPS, dissolved in 5 ml of ultrapure water. The reaction was carried out overnight. For purification, the particle dispersion was dialyzed against ultrapure water for 5 days, changing the water twice a day. The diameters and glass transition temperatures of the synthesized particles are summarized in table S1. Almost equal-sized particles with varying $n$-BA content have been synthesized (set-1, ~200 nm; set-2, ~420 nm).

### Crystal assembly
The colloidal crystals were fabricated by evaporation-induced self-assembly, by filtration, or by a combination of both techniques. Evaporation-induced self-assembly of a given amount of particle dispersion yields disk-shaped, highly crystalline colloidal monoliths with a diameter of ~20 mm. Particle assembly by filtration was carried out to fabricate multilayered, colloidal monoliths by sequential filtration of different particle dispersions. After the filtration of the last layer, the specimens were allowed to dry overnight under ambient conditions.

### Dynamic light scattering
Dynamic light scattering was performed on diluted particle dispersions on a Malvern Zetasizer with 175° backscattering geometry to obtain the hydrodynamic diameter and the size distribution of the synthesized particles.

### Light microscopy
The edges of the split colloidal crystals were investigated on a Carl Zeiss Axio Imager.A2m bright-field light microscope equipped with an AxioCam ICc 1 camera to study the macroscopic order within the fabricated colloidal monoliths.

### Scanning electron microscopy
SEM was performed on a Zeiss Leo 1530 electron microscope to obtain the hard sphere diameter of the particles. Furthermore, SEM images along the edges of the split colloidal crystals were obtained to get an idea of the particle ordering within the interior of the monoliths.

### Laser flash analysis

Laser flash analysis was conducted on a Linseis XFA 500 Xenon Flash apparatus equipped with an InSb infrared detector. The sample surfaces were coated with a thin layer of graphite (<15 μm) on the bottom and top sides. The measurements were conducted in helium atmosphere at a pressure of 980 mbar. The measurement was fitted with the radiation fit model provided by the software Aprosoft Laser Flash Evaluation v.1.06. Three measurements were performed at every temperature to obtain a mean thermal diffusivity of every individual sample. For data evaluation, the mean thermal diffusivity of three individual samples was taken into account. Because of the changes in thickness of the sample during sintering, the thickness of the samples has to be corrected accordingly. Further details are provided in the Supplementary Materials (39, 40).

### Density determination

The density of the pristine crystals was obtained by determining the mass and volume of the monoliths. The mass was obtained by weighing the crystals. The volume was determined on a Keyence VR-3100 3D digital macroscope. The density of the molten crystals was measured by a buoyancy balance according to the Archimedes principle.

### Differential scanning calorimetry

DSC was performed on a TA Instruments Q1000 differential scanning calorimeter according to ASTM E1269.

Three individual measurements were performed under a nitrogen flow of 50 ml min$^{-1}$ at a heating rate of 20 K min$^{-1}$. Two heating cycles were conducted between −40° and 200°C. The specific heat capacity was extracted from the second heating cycle.

## SUPPLEMENTARY MATERIALS

Supplementary material for this article is available at http://advances.sciencemag.org/cgi/content/full/3/11/eaao5238/DC1

Description of XFA evaluation

table S1. Hydrodynamic diameter $d_h$, polydispersity index (PDI), hard sphere diameter $d_{(sem)}$, and glass transition temperature $T_g$ of particles used in this study.

fig. S1. Temperature-dependent specific heat capacity of the investigated samples.

fig. S2. Temperature-dependent thickness and density of co-assembled colloidal crystals.

fig. S3. Temperature-dependent and thickness-corrected thermal diffusivity of the measured colloidal specimens.

fig. S4. Temperature-dependent thermal conductivity of coassembled colloidal crystals from two particles having a $T_g$ of ~61° and ~103°C.

fig. S5. Optical micrographs of a two-layer colloidal monolith made by filtration, and a two-layer monolith fabricated by a combination of evaporation-induced self-assembly and filtration.

fig. S6. SEM cross section images of the gradual film formation of crystalline binary assemblies.

## REFERENCES AND NOTES

1. V. Kubytskyi, S.-A. Biehs, P. Ben-Abdallah, Radiative bistability and thermal memory. *Phys. Rev. Lett.* **113**, 074301 (2014).
2. L. Wang, B. Li, Thermal memory: A storage of phononic information. *Phys. Rev. Lett.* **101**, 267203 (2008).
3. M. Wuttig, N. Yamada, Phase-change materials for rewriteable data storage. *Nat. Mater.* **6**, 824–832 (2007).
4. J. Zhu, K. Hippalgaonkar, S. Shen, K. Wang, Y. Abate, S. Lee, J. Wu, X. Yin, A. Majumdar, X. Zhang, Temperature-gated thermal rectifier for active heat flow control. *Nano Lett.* **14**, 4867–4872 (2014).
5. G. Wu, B. Li, Thermal rectification in carbon nanotube intramolecular junctions: Molecular dynamics calculations. *Phys. Rev. B* **76**, 085424 (2007).
6. C. W. Chang, D. Okawa, A. Majumdar, A. Zettl, Solid-state thermal rectifier. *Science* **314**, 1121–1124 (2006).
7. M. Liu, Y. Ma, H. Wu, R. Y. Wang, Metal matrix–metal nanoparticle composites with tunable melting temperature and high thermal conductivity for phase-change thermal storage. *ACS Nano* **9**, 1341–1351 (2015).
8. M. Chau, B. A. F. Kopera, V. R. Machado, S. M. Tehrani, M. A. Winnik, E. Kumacheva, M. Retsch, Reversible transition between isotropic and anisotropic thermal transport in elastic polyurethane foams. *Mater. Horiz.* **4**, 236–241 (2017).
9. H.-K. Lyeo, D. G. Cahill, B.-S. Lee, J. R. Abelson, M.-H. Kwon, K.-B. Kim, S. G. Bishop, B.-k. Cheong, Thermal conductivity of phase-change material Ge$_2$Sb$_2$Te$_5$. *Appl. Phys. Lett.* **89**, 151904 (2006).
10. M. Farhat, P.-Y. Chen, H. Bagci, C. Amra, S. Guenneau, A. Alù, Thermal invisibility based on scattering cancellation and mantle cloaking. *Sci. Rep.* **5**, 9876 (2015).
11. M. J. Dicken, K. Aydin, I. M. Pryce, L. A. Sweatlock, E. M. Boyd, S. Walavalkar, J. Ma, H. A. Atwater, Frequency tunable near-infrared metamaterials based on VO$_2$ phase transition. *Opt. Express* **17**, 18330–18339 (2009).
12. C. Dames, Solid-state thermal rectification with existing bulk materials. *J. Heat Transfer* **131**, 061301 (2009).
13. S. Kommandur, S. K. Yee, An empirical model to predict temperature-dependent thermal conductivity of amorphous polymers. *J. Polym. Sci. Part B Polym. Phys.* **55**, 1160–1170 (2017).
14. P. Ben-Abdallah, S.-A. Biehs, Near-field thermal transistor. *Phys. Rev. Lett.* **112**, 044301 (2014).
15. R. G. Moore, J. Zhang, V. B. Nascimento, R. Jin, J. Guo, G. T. Wang, Z. Fang, D. Mandrus, E. W. Plummer, A surface-tailored, purely electronic, Mott metal-to-insulator transition. *Science* **318**, 615–619 (2007).
16. T. Zhang, T. Luo, High-contrast, reversible thermal conductivity regulation utilizing the phase transition of polyethylene nanofibers. *ACS Nano* **7**, 7592–7600 (2013).
17. J. F. Ihlefeld, B. M. Foley, D. A. Scrymgeour, J. R. Michael, B. B. McKenzie, D. L. Medlin, M. Wallace, S. Trolier-McKinstry, P. E. Hopkins, Room-temperature voltage tunable phonon thermal conductivity via reconfigurable interfaces in ferroelectric thin films. *Nano Lett.* **15**, 1791–1795 (2015).
18. R. Chen, Y. Cui, H. Tian, R. Yao, Z. Liu, Y. Shu, C. Li, Y. Yang, T. Ren, G. Zhang, R. Zou, Controllable thermal rectification realized in binary phase change composites. *Sci. Rep.* **5**, 8884 (2015).
19. P. C. Sun, Y. L. Wu, J. W. Gao, G. A. Cheng, G. Chen, R. T. Zheng, Room temperature electrical and thermal switching CNT/Hexadecane composites. *Adv. Mater.* **25**, 4938–4943 (2013).
20. R. Zheng, J. Gao, J. Wang, G. Chen, Reversible temperature regulation of electrical and thermal conductivity using liquid–solid phase transitions. *Nat. Commun.* **2**, 289 (2011).
21. Y. Li, X. Shen, Z. Wu, J. Huang, Y. Chen, Y. Ni, J. Huang, Temperature-dependent transformation thermotics: From switchable thermal cloaks to macroscopic thermal diodes. *Phys. Rev. Lett.* **115**, 195503 (2015).
22. M. D. Losego, I. P. Blitz, R. A. Vaia, D. G. Cahill, P. V. Braun, Ultralow thermal conductivity in organoclay nanolaminates synthesized via simple self-assembly. *Nano Lett.* **13**, 2215–2219 (2013).
23. W.-L. Ong, S. M. Rupich, D. V. Talapin, A. J. H. McGaughey, J. A. Malen, Surface chemistry mediates thermal transport in three-dimensional nanocrystal arrays. *Nat. Mater.* **12**, 410–415 (2013).
24. T. Still, W. Cheng, M. Retsch, U. Jonas, G. Fytas, Colloidal systems: A promising material class for tailoring sound propagation at high frequencies. *J. Phys. Condens. Matter* **20**, 404203 (2008).
25. T. Still, W. Cheng, M. Retsch, R. Sainidou, J. Wang, U. Jonas, N. Stefanou, G. Fytas, Simultaneous occurrence of structure-directed and particle-resonance-induced phononic gaps in colloidal films. *Phys. Rev. Lett.* **100**, 194301 (2008).
26. T. Still, M. Retsch, U. Jonas, R. Sainidou, P. Rembert, K. Mpoukouvalas, G. Fytas, Vibrational eigenfrequencies and mechanical properties of mesoscopic copolymer latex particles. *Macromolecules* **43**, 3422–3428 (2010).
27. S. G. Johnson, J. D. Joannopoulos, J. N. Winn, R. D. Meade, *Photonic Crystals: Molding the Flow of Light*. (Princeton Univ. Press, 2008).
28. W. Cheng, J. Wang, U. Jonas, G. Fytas, N. Stefanou, Observation and tuning of hypersonic bandgaps in colloidal crystals. *Nat. Mater.* **5**, 830–836 (2006).
29. E. Alonso-Redondo, M. Schmitt, Z. Urbach, C. M. Hui, R. Sainidou, P. Rembert, K. Matyjaszewski, M. R. Bockstaller, G. Fytas, A new class of tunable hypersonic phononic crystals based on polymer-tethered colloids. *Nat. Commun.* **6**, 8309 (2015).
30. K. R. Phillips, G. T. England, S. Sunny, E. Shirman, T. Shirman, N. Vogel, J. Aizenberg, A colloidoscope of colloid-based porous materials and their uses. *Chem. Soc. Rev.* **45**, 281–322 (2016).
31. N. Vogel, M. Retsch, C.-A. Fustin, A. del Campo, U. Jonas, Advances in colloidal assembly: The design of structure and hierarchy in two and three dimensions. *Chem. Rev.* **115**, 6265–6311 (2015).
32. M. Retsch, Z. Zhou, S. Rivera, M. Kappl, X. S. Zhao, U. Jonas, Q. Li, Fabrication of large-area, transferable colloidal monolayers utilizing self-assembly at the air/water interface. *Macromol. Chem. Phys.* **210**, 230–241 (2009).
33. F. A. Nutz, P. Ruckdeschel, M. Retsch, Polystyrene colloidal crystals: Interface controlled thermal conductivity in an open-porous mesoparticle superstructure. *J. Colloid Interface Sci.* **457**, 96–101 (2015).

34. J. D. Joannopoulos, P. R. Villeneuve, S. Fan, Photonic crystals: Putting a new twist on light. *Nature* **386**, 143–149 (1997).

35. Y. N. Xia, B. D. Gates, Y. Yin, Y. Lu, Monodispersed colloidal spheres: Old materials with new applications. *Adv. Mater.* **12**, 693–713 (2000).

36. F. A. Nutz, M. Retsch, Interfacial and volumetric sensitivity of the dry sintering process of polymer colloidal crystals: A thermal transport and photonic bandgap study. *Phys. Chem. Chem. Phys.* **19**, 16124–16130 (2017).

37. J. W. Goodwin, J. Hearn, C. C. Ho, R. H. Ottewill, Studies on the preparation and characterisation of monodisperse polystyrene laticee. *Colloid Polym. Sci.* **252**, 464–471 (1974).

38. R. H. Ottewill, J. N. Shaw, Studies on the preparation and characterization of monodisperse polystyrene latices. *Kolloid Z. Z. Polym.* **215**, 161–166 (1967).

39. L. Dusza, Combined solution of the simultaneous heat loss and finite pulse corrections with the laser flash method. *High Temp.-High Press.* **27**, 467–473 (1995).

40. W. J. Parker, R. J. Jenkins, C. P. Butler, G. L. Abbott, Flash method of determining thermal diffusivity, heat capacity, and thermal conductivity. *J. Appl. Phys.* **32**, 1679–1684 (1961).

**Citation:** F. A. Nutz, M. Retsch, Tailor-made temperature-dependent thermal conductivity via interparticle constriction. *Sci. Adv.* **3**, eaao5238 (2017).